AIChE

Droplets Sliding Over Shearing Surfaces Studied by Molecular Dynamics

J. J. Derksen
Chemical Engineering, Delft University of Technology, Julianalaan 136, 2628 BL Delft, The Netherlands

DOI 10.1002/aic.14930

Through molecular dynamics, the sliding motion of a liquid drop embedded in another liquid over a substrate as a result of a shear flow is studied. The two immiscible Lennard-Jones liquids have the same density and viscosity. The system is isothermal. Viscosity, surface tension, and static contact angles follow from calibration simulations. Sliding speeds and drop deformations (in terms of dynamic contact angles) are determined as a function of the shear rate. The latter is nondimensionalized as a capillary number (Ca) that has been varied in the range 0.02–0.64. For Ca up to 0.32, sliding speeds are approximately linear in Ca. For larger Ca, very strong droplet deformations are observed.

Keywords: wetting, immiscible liquids, surface tension, moving contact lines, molecular dynamics, Lennard-Jones liquid

Introduction

Pore-scale phenomena in oil recovery and CO_2 storage,[1,2] separation in membranes,[3] manipulation of minute amounts of liquids on patterned surfaces,[4] and nanofluidics-based medical diagnostics[5] are examples of nanoscale flow and transport processes. Oil recovery and CO_2 storage in rock formations highlight the often multiphase character (gas-liquid mixtures or systems with multiple immiscible liquids—oil, water, pressurized CO_2) of many such systems. To control and steer motion of fluids in very confined spaces, quantifying the dynamical interaction of the phases with one another and with enclosing walls is essential. Surface phenomena—surface tension, adhesion forces—play a crucial role in these dynamics.

In this article, motivated by the aim to elucidate pore-scale processes in oil reservoirs, we study through molecular dynamics (MD) simulations the interaction between viscous forces brought about by a shearing motion, forces due to surface tension, and wall adhesion forces in geometrically simple systems containing two immiscible liquids. The main question to be addressed in this article is to what extent the shearing motion of a continuous phase liquid is able to mobilize a nanosize liquid drop attached to a solid substrate. For simplicity, the two liquids (the drop and the continuous phase) have the same density and viscosity. There is a surface tension between the liquids and the liquids interact—in general—with different strengths with the substrate. There are two reasons for performing MD simulations in this study. In the first place, the size of the (nano) pores makes MD a directly applicable approach: the number of molecules in a representative portion of the pore can be well dealt with in an MD simulation (demonstrated by earlier studies in this field, e.g., Refs. 6 and 7). In the second place, we want to generate results with MD simulations that might be compared with simulations based on continuum assumptions of the fluids involved. Continuum approaches are desirable as they are computationally less intensive and thus have the advantage of being able to handle larger portions of pore networks so that they are able to capture effects of geometrical complexity such as the tortuosity and the branching characteristics of pore systems. One of the intricate issues in the systems we study, however, is three-phase (solid–liquid–liquid) contact lines and their motion over solid surfaces. For describing this motion, continuum methods need dedicated models,[8] whereas in MD simulations such slip would naturally occur given a set of molecular interaction parameters. The MD simulations reported here are not based on a specific but rather on a more generic liquid-liquid-solid system; we use Lennard-Jones (LJ) liquids as Newtonian model fluids and characterize them mainly by continuum-type material parameters such as viscosity, surface tension, density, and contact angle with a solid surface.

There is, of course, a vast literature on MD simulations in general and of MD of LJ fluids in particular. A number of textbooks[9,10] provide excellent introductions to MD and show its versatility in a massive spectrum of applications. Since its inception in the mid-50s of the previous century,[11] MD has found widespread use in many disciplines in science and engineering. Trends and applications in chemical engineering have been reviewed recently.[12–14] Limiting this brief literature review to topics most relevant to the current paper (MD of LJ fluids, drops on substrates, and pore-scale modeling in oil recovery), there is significant activity over the past 10 years. Phase behavior of LJ fluids,[15] their transport coefficients,[16] and their interaction with solid substrates[17–19] have been reported in a variety of ways and situations, including deformation of drops on surfaces due to force fields.[20] Interaction between liquids and substrates is also of key importance in the formation and rupture of liquid bridges.[21,22] As noted above,

---

Correspondence concerning this article should be addressed to J. J. Derksen at j.j.derksen@tudelft.nl.

Boek and coworkers are prominent in the application of MD simulations in the field of (enhanced) oil recovery.[6,7]

This article is organized along the following lines: in the next section, the model system, its geometry, the simulation approach, and the (dimensionless) parameter space covered are introduced. Then, calibrations for viscosity, surface tension, and contact angle are described. The results of the actual simulations comprise deformation and sliding speeds of drops over a substrate as a result of an imposed simple shear flow. The final section summarizes the main conclusions drawn from these results.

Model System and Simulation Method

Model system

The model system consists of truncated and shifted LJ (LJTS) fluids confined between two parallel solid plates that make a shearing motion, that is, the plates move in opposite directions, parallel to themselves, see Figure 1. The figure also specifies the dimensions of the computational domain, and a coordinate system that will be used throughout this article. Fully periodic boundary conditions apply.

The pairwise LJ interaction potential u_{ij}^{LJ} is written as

$$u_{ij}^{\mathrm{LJ}}\left(r_{ij}\right)=4\varepsilon\left[\left(\sigma/r_{ij}\right)^{12}-d_{\alpha\beta}\left(\sigma/r_{ij}\right)^{6}\right] \tag{1}$$

with r_{ij} the separation between molecule i and j, and σ and ε the molecular length and energy scale, respectively. The parameter $d_{\alpha\beta}$[23] controls the interaction between the three phases present in the system: two immiscible liquids and a solids phase. Molecules belonging to the same phase interact with $d_{\alpha\alpha}=1$. The molecules of the disperse liquid phase (the droplet) and the continuous liquid phase interact according to $d_{\mathrm{cd}}=0.6$. As we will see, this creates surface tension between the two immiscible liquids. The two liquids have the same viscosity and density. The continuous phase liquid interacts with the solid with $d_{\mathrm{cs}}=0.7$. The interaction parameter between the disperse phase liquid and the solid has been varied (in the range $0.5 \leq d_{\mathrm{ds}} \leq 0.9$) to vary the contact angle of the drop on the substrate. The LJ interaction potential has been truncated at 2.5σ and shifted so that eventually the molecules interact according to $u_{ij}\left(r_{ij}\right)=u_{ij}^{\mathrm{LJ}}\left(r_{ij}\right)-u_{ij}^{\mathrm{LJ}}(2.5\sigma)$, $r_{ij}<2.5\sigma$ and $u_{ij}\left(r_{ij}\right)=0$, $r_{ij} \geq 2.5\sigma$.

The two plates consist of molecules arranged in an FCC lattice with the [100] surface in contact with the liquid. The lattice parameter is 1.55σ. The thickness of the solid plates is larger than the cutoff distance of 2.5σ. The plates are rigid, which means that the molecules in each plate move with the same, imposed velocity, the upper ones in the positive x direction, and the lower ones in negative x-direction; they do not undergo thermal motion.

The system is initialized by placing the liquid molecules on a simple cubic lattice in between the plates, giving them random velocities, and assigning the molecules that fall within a half-sphere with radius $R_0=20.4\sigma$ centred around the middle of the bottom plate to the disperse phase; the rest of the molecules belong to the continuous phase. The density of the liquids is $\rho^* \equiv \rho\sigma^3=0.84$. Velocity scaling[18] is used to maintain a constant temperature of $T^* \equiv k_{\mathrm{B}}T/\varepsilon=0.68$ (with k_{B} the Boltzmann constant). Before starting the shearing motion, the system is first equilibrated over a time period of at least $t_{\mathrm{eq}}^* \equiv t_{\mathrm{eq}}(\varepsilon/m)^{1/2}/\sigma=460$ (m is the mass of a molecule; all molecules have the same mass). The situation at the end of the equilibration period is used to determine the static contact angle (more details about this in the next section).

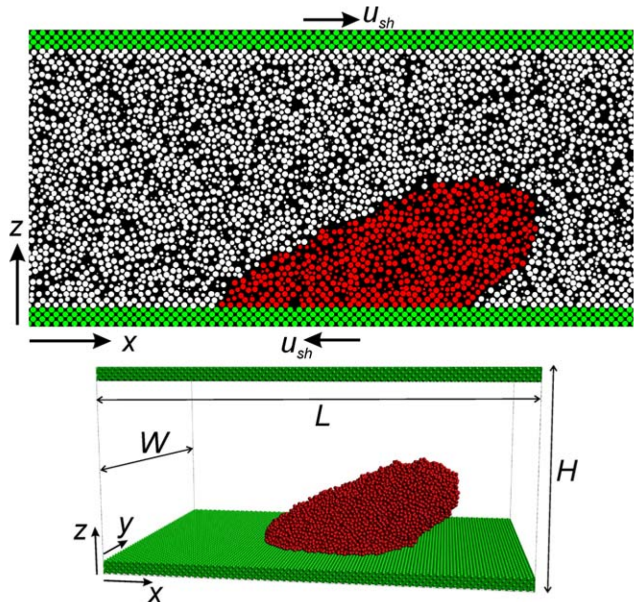

Figure 1. Simulation domain and coordinate system.

Top: Cross section at $y=W/2$; green is solid, white is continuous phase liquid, red is disperse phase liquid; all particles have the same size. Bottom: A three-dimensional view with the same color coding and the continuous phase liquid invisible. The shearing motion is indicated by the velocity vectors $\boldsymbol{u}_{\mathrm{sh}}$. $L^* \equiv L/\sigma=102$, $H^*=50$, $W^*=68$. [Color figure can be viewed in the online issue, which is available at wileyonlinelibrary.com.]

An in-house (Fortran) computer code is used to perform the simulations. A link-list efficiently identifies interacting particle pairs. Once the interaction forces on each particle have been determined, we perform a leapfrog velocity and position update.[9] The time step is $\Delta t^*=0.0046$. In a typical simulation, the number of dispersed phase molecules is 16,000, the number of continuous phase molecules 240,000, and the number of solid molecules 46,000.

Parameter space

The simulations have been performed at fixed temperature $T^*=0.68$ and density $\rho^*=0.84$. The main dimensionless input variable governing the deformation of the drop in shear is the capillary number $\mathrm{Ca} \equiv \rho\nu GR_0/\gamma$, with ν the kinematic viscosity of the liquids, G the shear rate, and γ the surface tension between the two liquids. The static contact angle is the second dimensionless input variable.

As already mentioned, the density ratio and viscosity ratio of the two liquids have been set to one for simplicity. As we will see, the Reynolds number based on initial drop radius and shear rate ($Re \equiv GR_0^2/\nu$) is smaller than 1 in all cases which signifies the minor relevance of inertial effects in our study.

Calibrations

A number of calibration simulations have been carried out to determine viscosity, surface tension, and static contact angle for the molecular system at hand at the given (and fixed) temperature and density.

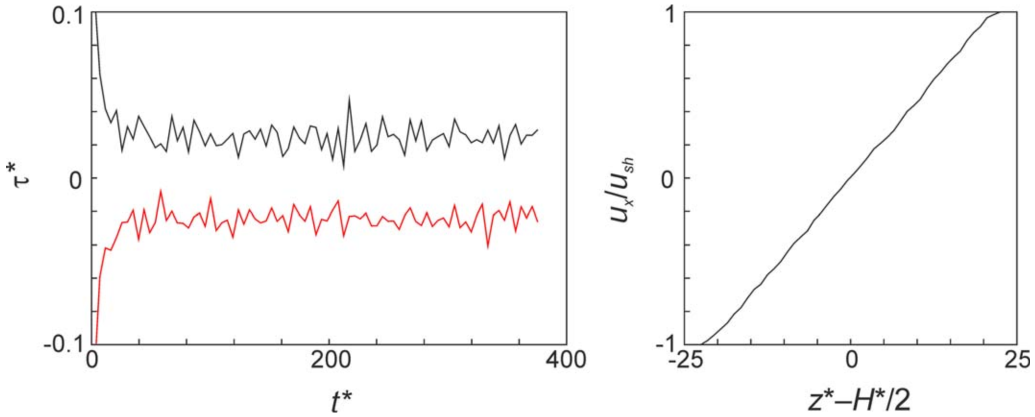

Figure 2. Left: Time series of the shear stress $\tau^* \equiv \tau\sigma^3/\varepsilon$ on the top (black) and bottom (red) solid wall in a single-phase shear simulation; each data point is the average of 1000 time steps with $\Delta t^* = 0.0046$. Right: Average wall-normal *x*-velocity profile. In this case, $u^*_{sh} \equiv u_{sh}\sqrt{m/\varepsilon} = 0.14$.

[Color figure can be viewed in the online issue, which is available at wileyonlinelibrary.com.]

Viscosity

The same shear cell as defined in Model System and Simulation Method Section is now filled with a single-phase liquid. Its viscosity is estimated from the shear force on the plates to maintain a shearing motion and the average velocity profile in the liquid. Figure 2a shows a time series of the average shear stress on the upper and lower plate. The system is started (at $t = 0$) by impulsively switching on the shearing motion of the plates from an equilibrated situation with zero shear. As can be seen, a steady state sets in after $t^* \approx 50$. In Figure 2b, the average shear velocity profile is shown, averaged over the two homogeneous directions (x and y) and over time (in the period $80 \leq t^* \leq 380$). From the time-averaged shear stress and the slope of the linear part of the velocity profile, the viscosity is determined: the data in Figure 2 imply an average stress of $\bar{\tau}^* = 0.0245$; the average shear rate is $G^* \equiv G\sqrt{m/\varepsilon\sigma} = 0.00667$. As a result, the dynamic viscosity is $\mu^* = \bar{\tau}^*/G^* = 3.67$. This is well in line with viscosity results presented by Ref. 16; at $T^* = 0.7$ and $\rho^* = 0.85$, their figure 7 indicates $\mu^* \approx 3.5$. The kinematic viscosity is $v^* \equiv v\sqrt{m/\varepsilon}/\sigma = 4.37$. Based on the latter value, momentum penetration over half the channel height $H^*/2 = 25$ takes $t^* = \frac{H^{*2}}{4\pi v^*} \approx 50$ which agrees well with the length of the transient phase as observed in Figure 2a.

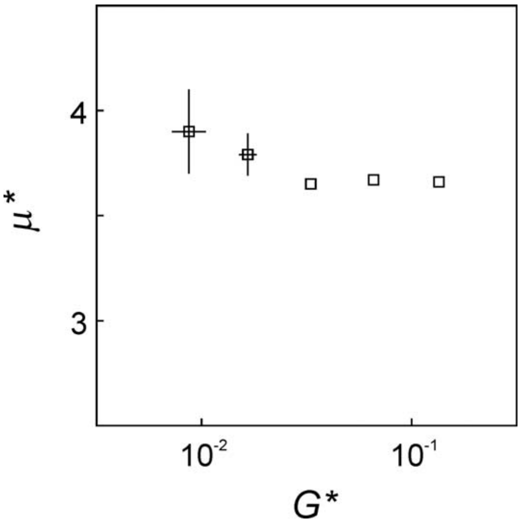

Figure 3. Dynamic viscosity as a function of shear rate.

On data points without error bars, the uncertainty is less than the symbol size.

This procedure for determining the viscosity has been repeated for a number of shear rates to confirm the Newtonian character of the liquid, see Figure 3. The increase in statistical uncertainty for the lower shear rates is a result of the relatively higher levels of fluctuations (in average velocity and shear stress) at low shear and the for all cases fixed time interval over which averaging takes place.

Surface tension

Two types of simulations have been performed to estimate the surface tension between the two liquids. The first estimate is based on planar interfaces and the "virial route"[10,24]: the two liquids are placed in equal amounts in a cubic, fully periodic domain with two interfaces coinciding with yz planes; there are no solid walls (see Figure 4c). Temperature and density are set to the default values of $T^* = 0.68$ and $\rho^* = 0.84$. After equilibration, surface tension is determined according to[24]

$$\gamma = \frac{1}{2A}\left\langle \sum_{i=1}^{N}\sum_{j>i}^{N}\left(1-3x_{ij}^2/r_{ij}^2\right) r_{ij}\frac{\partial u\left(r_{ij}\right)}{\partial r_{ij}}\right\rangle \qquad (2)$$

with N the total number of particles, and A the surface area of the yz plane (the factor 2 in front of A is because there are two interfaces). The angled brackets indicate ensemble averaging which in practice is done by averaging over many realizations that were collected after equilibration.

The cubic domain has side length $L^* = 43$ and contains 67,200 molecules with equal amounts for each liquid. The system is equilibrated over a time $t^* = 600$. Applying Eq. 2 over a set of 200 independent realizations results in $\gamma^* = 1.55 \pm 0.05$ where the uncertainty has been estimated from using different sets of realizations in the ensemble.

In the second approach for determining surface tension, the system is initialized differently. Again there is a fully periodic, three-dimensional cubic domain (with side length $L^* = 60$), see Figure 4b. In the center, a spherical droplet is placed. After equilibration, the radial pressure profile is calculated. The pressure difference over the interface Δp and the radius of the drop R then determines the surface tension (Young–Laplace equation): $\gamma = \frac{1}{2}\Delta pR$. The pressure distribution is determined in a volumetric way.[25] The average pressure in a volume Ω is

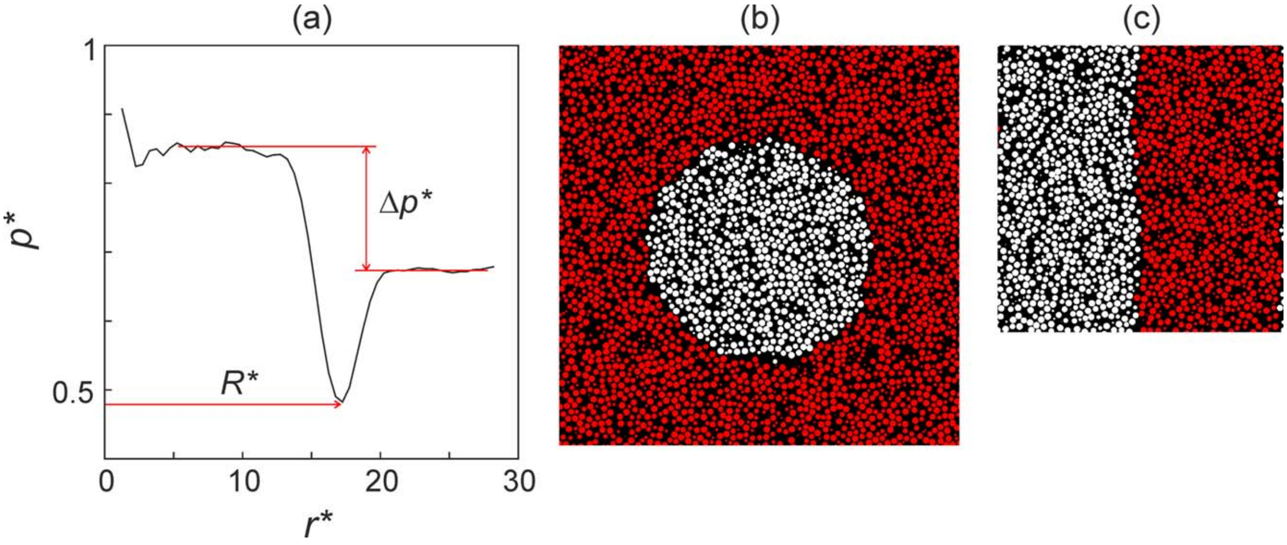

Figure 4. Determining surface tension. (a) Radial pressure profile (with resolution $\Delta r^* = 2.5$) inside and outside the drop a cross section of which is shown in (b). (c) Cross section through the simulation domain for determining surface tension of a planar interface via the virial route.

[Color figure can be viewed in the online issue, which is available at wileyonlinelibrary.com.]

$$p=\frac{1}{3\Omega}\left\langle \sum_{i=1}^{N}\Lambda_i m|\mathbf{v_i}|^2-\sum_{i=1}^{N}\sum_{j>i}^{N}\ell_{ij}r_{ij}\frac{\partial u(r_{ij})}{\partial r_{ij}}\right\rangle \tag{3}$$

with N the total number of molecules, Λ_i equal to 1 if the center of molecule i falls within Ω and 0 otherwise; ℓ_{ij} the fraction of the line connecting molecules i and j that falls within Ω; and $\mathbf{v_i}$ the velocity of molecule i. Concentric spherical shells with thickness $\Delta r^* = 2.5$ were taken as the volumes in which the average pressure was determined. A cross section through the simulation domain and a typical radial pressure profile are shown in Figures 4b, a, respectively. From this pressure profile, a surface tension of $\gamma^* = 1.53 \pm 0.1$ has been estimated. As can be judged from the profile, there is some uncertainty in the pressure levels inside and outside of the drop as well as in the radius of the equilibrated drop which is reflected in the ± 0.1 margin that we report.

For the purpose of determining capillary numbers, in the remainder of this article, the surface tension between the two liquids will be assumed to be $\gamma^* = 1.54$ with the realization that this is order 10% accurate.

Static contact angle

By varying the interaction parameter d_{ds} between the disperse phase liquid and the solid while keeping that of the continuous phase liquid with the solid constant ($d_{\mathrm{cs}} = 0.7$), drops with different static contact angle on the substrate are created. Figure 5 shows their time-averaged shape, including estimates of the contact angle. Each of the drops shown in the figure is initialized as a hemisphere with radius $R_0^* = 20.4$ in contact with the substrate so that each drop has the same volume. Note that R_0 is the length scale, that is, used when determining the capillary number. These systems are equilibrated over $t^* = 460$. The time averages shown in Figure 5 were collected over a subsequent period $t^* = 460$. As has been observed in earlier studies,[18] layering occurs near the substrate, most visible for the drops with the smaller contact angles. When fitting a circular arc to the interface to determine the static contact angle, the part of the interface near the substrate is discarded. The fitting procedure will be discussed in detail in Results Section where the more general case of deformed drops is considered. The angle with which the arc intersects with the top surface of the substrate is our estimate for the static contact angle. In this study, it varies between $\theta = 65°$ and $111°$.

Results

The main interest of this study is deformation and sliding of drops over a substrate as a result of a shear flow. The main dependencies to be studied are those with the capillary number $\mathrm{Ca} \equiv \rho v G R_0/\gamma$ and the static contact angle θ. The five equilibrated, static droplets as depicted in Figure 5 are the starting points for the shear simulations. At $t = 0$, the plates impulsively start moving in opposite direction. The capillary number has been varied—between 0.02 and 0.64—by varying the shear rate G; the other parameters defining Ca have not been

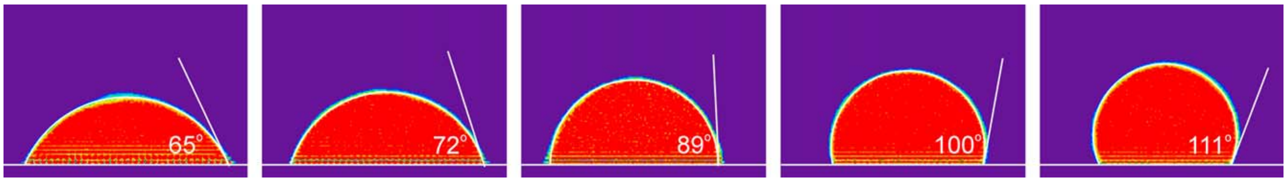

Figure 5. Equilibrated droplet shapes and contact angle estimates.

In all cases, $d_{\mathrm{cs}} = 0.7$ (see Eq. 1). From left to right, $d_{\mathrm{ds}} = 0.9, 0.8, 0.7, 0.6, 0.5$. The white curve is the best fit of a circular arc (with its center x-location at $x = 0.5L$ and its radius and center z-location as fitting parameters) to the interface. [Color figure can be viewed in the online issue, which is available at wileyonlinelibrary.com.]

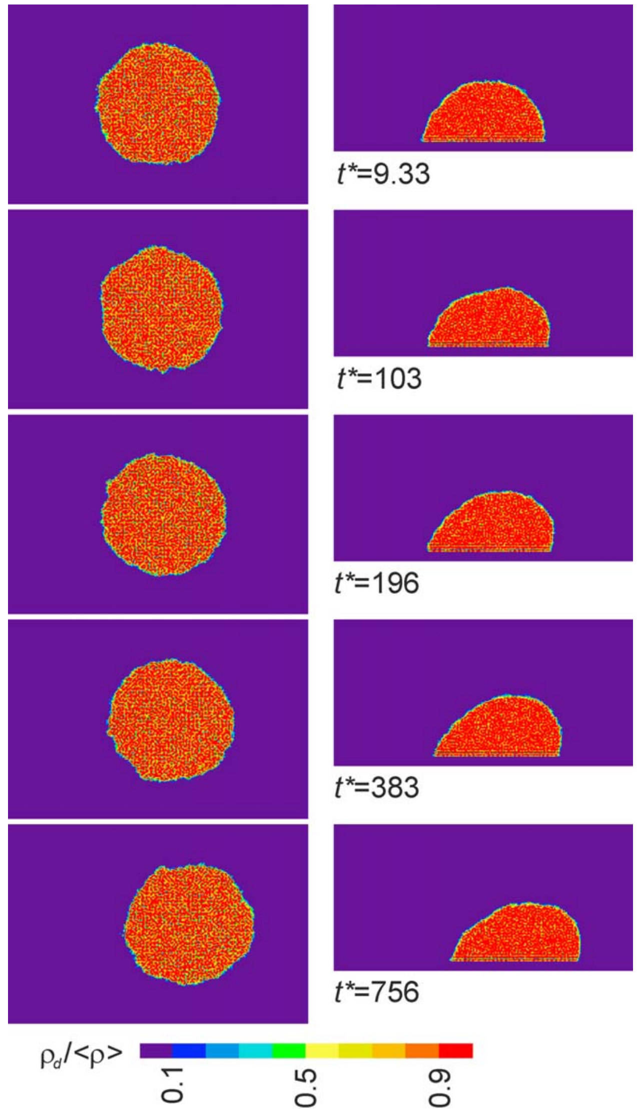

Figure 6. Evolution of a shear simulation at Ca = 0.16 in terms of dispersed (drop) phase density contours.

Left column: *xy* cross sections directly above the substrate (footprint of the drop); right column: Symmetry plane *xz* cross sections. Time increases from top to bottom. Each panel is a time average over an interval $\Delta t^* = 19.7$. The time reported per panel corresponds to the middle of the time averaging interval. The drop has static contact angle $\theta = 89^{\text{o}}$. [Color figure can be viewed in the online issue, which is available at wileyonlinelibrary.com.]

varied. The consequence of this strategy is that also the Reynolds number varies. The maximum Reynolds number is 0.6 which is considered sufficiently low to discard inertial effects. Uncertainty in Ca is mainly due to uncertainties in v (approximately 5%) and γ (10%) and thus is approximately 15%.

The way the droplets are analyzed will be demonstrated for drops which have a static contact angle of $\theta = 89^{\text{o}}$. In Figure 6, we show cross sections through these drops in a reference frame moving with the lower plate. The *xy* cross sections closely above this plate (showing the "footprint" of the drop) indicate a slight motion to the right which indicates that the drop is sliding over the lower plate due to the shear flow. In this process of sliding, the drop's footprint remains approximately circular. The *xz* cross sections (right column of panels in Figure 6) show the deformation of the drop. Beyond $t^* \approx 100$, the drop does not change shape anymore and a (dynamic) steady state sets in.

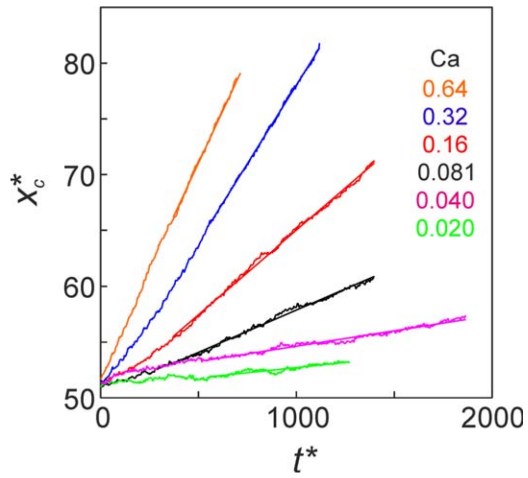

Figure 7. Footprint center position (x_c^*) as a function of time for various capillary numbers.

The straight lines are best fits through the data points and have been used for estimating the average sliding velocity. All cases have $\theta = 89^{\text{o}}$. [Color figure can be viewed in the online issue, which is available at wileyonlinelibrary.com.]

Sliding speeds have been estimated by tracking the center of mass of the footprint as a function of time, see Figure 7. After an initialization stage, these time traces get approximately linear. A least squares fit with a straight line (fits also shown in Figure 7) then provide an estimate for the average sliding speed. An overview of the average sliding speeds of all simulations is shown in Figure 8. This figure shows that to a fair approximation and for Ca ≤ 0.32, the sliding speed is linear with the capillary number. As the capillary number has been varied by varying the shear rate G, this implies a fixed velocity ratio $\frac{v_{\text{slide}}}{GR_0}$ for each of the drops. Figure 9 shows this velocity ratio as a function of the static contact angle: the higher the static contact angle, the more the drop is susceptible to the shearing motion and thus the faster it slides over the substrate.

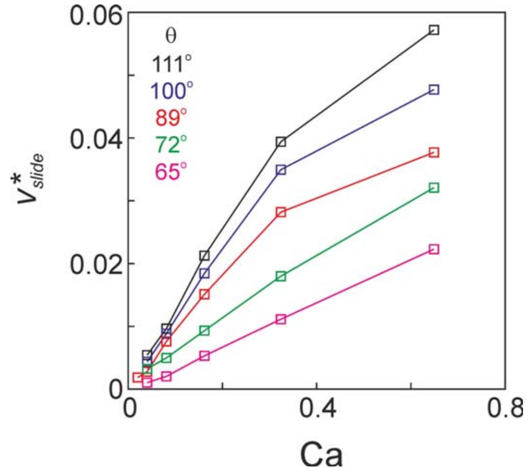

Figure 8. Steady-state droplet sliding velocity as a function of the capillary number for droplets that have static contact angle θ as indicated.

[Color figure can be viewed in the online issue, which is available at wileyonlinelibrary.com.]

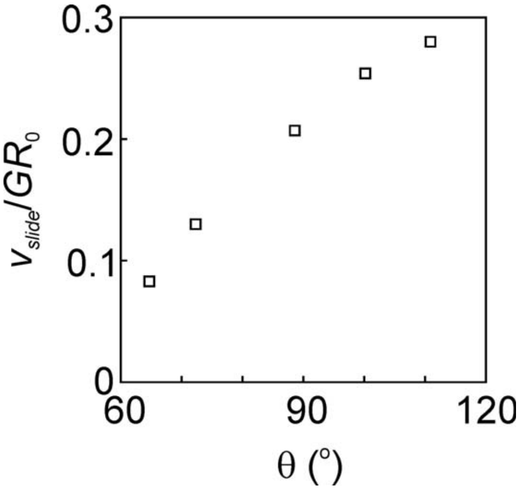

Figure 9. Sliding velocity relative to shear rate times initial drop radius as a function of the static contact angle θ.

The linear trend between sliding speed and capillary number is not continued until the highest capillary number (Ca = 0.64); at this level of Ca, sliding speeds fall below the linear trend, the more so for the larger static contact angles. As we will see, Ca = 0.64 is a special situation for which the drops—at least within the limits of our computations—do not reach a steady shape; they keep deforming while sliding over the substrate with an approximately constant velocity.

For Ca $\leq$ 0.32, a steady drop shape is eventually reached. These shapes are shown in Figure 10. This figure shows drop shapes averaged over a time period of at least $t^* = 460$ (100,000 time steps) where in the averaging process, we move with the (sliding) drop. The stronger the liquid shear, the stronger the for-aft asymmetry. To characterize the latter, a receding and advancing contact angle (θ_r and θ_a, respectively) have been defined. They are determined by fitting circles to portions of the liquid-liquid interface,[26] see Figure 11, with the interface defined as the location with $\rho_d/\langle\rho\rangle = 0.5$. The angle with which the fitted circles intersect the top of the substrate is then measures for the contact angles. The parts of the interface close to the substrate where layering occurs (most notable in Figure 10 for $\theta = 65^o$) are discarded from the fitting process. The same procedure was followed for determining static contact angles (Figure 5), except that then a single circle was fit to the interface.

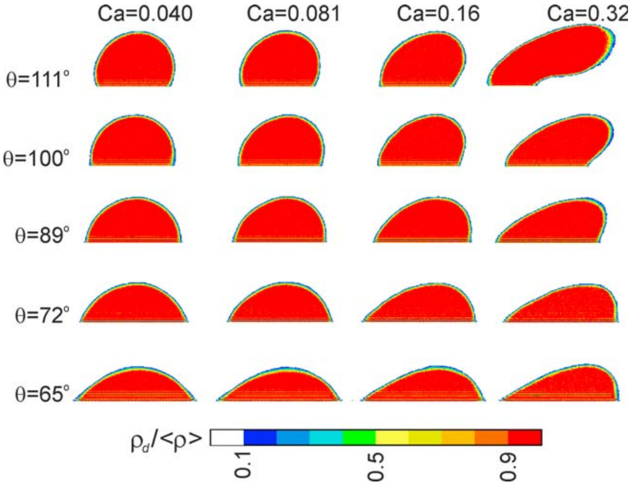

Figure 10. Time-averaged shape of sliding droplets.

[Color figure can be viewed in the online issue, which is available at wileyonlinelibrary.com.]

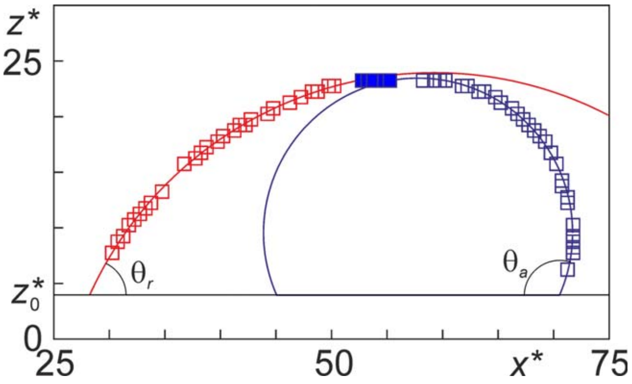

Figure 11. Fitting procedure for determining the receding and advancing contact angles (θ_r and θ_a, respectively).

The square symbols are locations in the density contour plot (see Figure 9) on the curve $\rho_d/\langle\rho\rangle = 0.5$; the red circle segment is a least squares fit through the red open symbols; the blue circle segment is a least squares fit through the open blue symbols. The filled symbols do not take part in the fitting process. The reference level for determining contact angles z_0^* is one diameter above the center location of the top level molecules of the substrate. In this example: Ca = 0.081, $\theta = 89^\circ$. [Color figure can be viewed in the online issue, which is available at wileyonlinelibrary.com.]

For most of the drop shapes in Figure 10, one then can quantify how advancing and receding contact angles depend on the capillary number, see Figure 12. The main trend is that the difference $\theta_a - \theta_r$ is a strong function of the capillary number. For situations where the advancing side of the droplet has a complex shape with, for example, curvature changing sign, θ_a could not be determined. This is illustrated in the inset of panel $\theta = 100^o$ of Figure 12 where it shows that the right circle cannot accurately describe the advancing side of the drop which leads to a significant overestimation of θ_a. Similar difficulties apply to determining θ_r for cases with relatively high Ca and small static contact angle θ. Then, curvature changes strongly over short distances above the substrate which already is a problematic region for fitting given the effect of layering.

No steady droplet shape could be established for Ca = 0.64; the drop keeps on stretching. Once its length is comparable with the length L of the domain, the drop starts interacting with itself over the periodic boundaries which is physically unrealistic. In Figure 13, some of the later stages of these high Ca simulations are shown with interesting features, such as the drop's footprint being very different for different static contact angles and the extreme extension of the drop. These results for Ca = 0.64 clearly are preliminary. They have been included in this article to highlight the departure from linearity, see Figure 8, for capillary numbers above some threshold. We leave a more systematic study of such nonlinear effects for future work (that clearly needs longer simulation domains).

Conclusions

Sliding and deformation of a liquid drop on a substrate as a result of shear of a surrounding liquid has been studied by

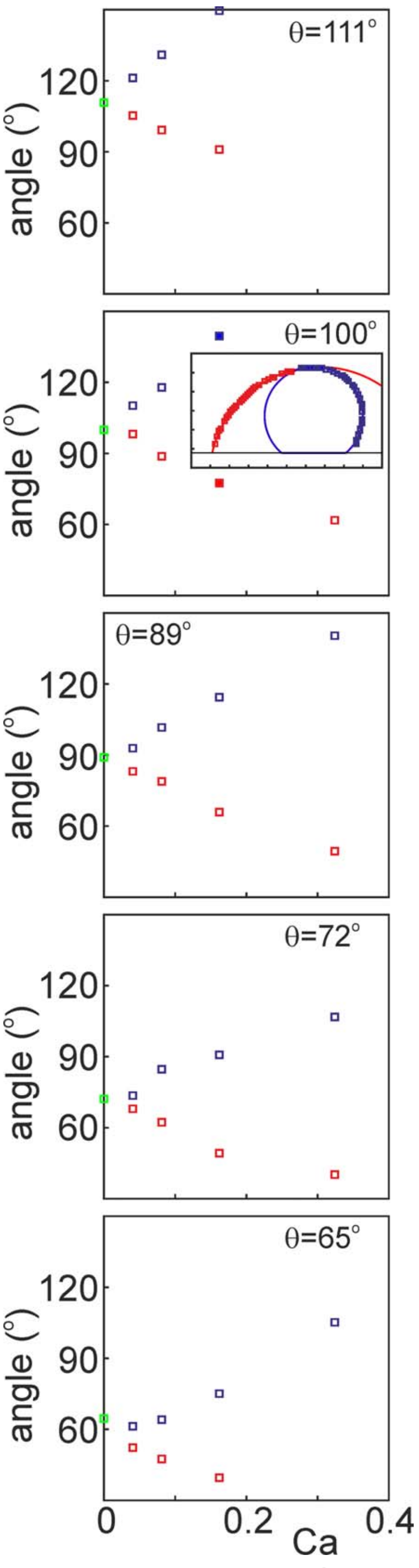

Figure 12. Receding contact angle θ_r (red symbols) and advancing angle θ_a (blue symbols) as a function of Ca for all static contact angles θ (green symbols) investigated.

The inset in the second panel from the top relates to the filled data points in that panel and is discussed in the text. [Color figure can be viewed in the online issue, which is available at wileyonlinelibrary.com.]

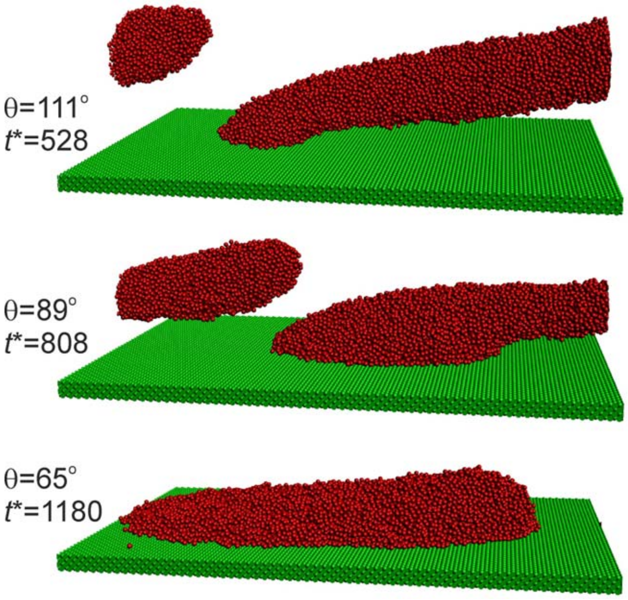

Figure 13. Impressions of drop deformation at Ca = 0.64 for three static contact angles.

Instantaneous realizations at indicated moments. Note the periodicity of the computational domain. [Color figure can be viewed in the online issue, which is available at wileyonlinelibrary.com.]

means of MD simulations. The two immiscible LJ liquids involved have the same density and viscosity. Surface tension between them is the result of a weaker attractive part of the interaction potential between unlike molecules as compared with like molecules. The main dimensionless parameter controlling the drop deformation is the capillary number (Ca) that can be interpreted as the ratio between (deforming) viscous forces and (restoring) forces due to surface tension. Next to Ca, the second variable whose influence on sliding and deformation has been studied is the static contact angle of the drop on the substrate.

First-calibration simulations were performed to determine transport coefficients and material properties of the actual system that in the MD simulations is only defined in terms of interaction potentials, overall density, temperature, and the structure and density of the substrate. The viscosity calibration showed favorable agreement with what is known from the literature.[16] The surface tension was determined by two methods (the virial route and the Young–Laplace law) that showed a consistent outcome. Variation in static contact angle (between 65 and 110°) was achieved by changing the interaction strengths between liquid and substrate molecules.

Over the entire capillary number range considered ($0.02 \leq \text{Ca} \leq 0.64$), the drop was sliding over the substrate. For $\text{Ca} \leq 0.32$, the sliding speed was proportional to the shear rate with a proportionality constant that was dependent on the static contact angle of the drop: an increasing contact angle increases the sliding speed as the drop protrudes further into the shear flow. Dependent on the static contact angle, the sliding speed is between 10 and 30% of shear rate times (initial) drop radius. The deformation of the drop under shear was quantified—where possible—with receding and advancing dynamic contact angles with the difference between the two increasing with increasing Ca.

The highest capillary number studied (Ca = 0.64) showed very strong deformation and deviation from the linearity between sliding speed and shear rate. This high end of the capillary number is worthwhile investigating further with more intensive calculations in larger domains to better accommodate strong drop deformation.

There are many more avenues for future research. In the first place experimental validation, where it is not directly necessary to go down to the—in principle—very small scales considered in this article (if $\sigma = O(1\ \text{nm})$, drop radii would be order 20 nm). We hypothesize that, given our generic approach, much larger drops in experiments behave similar (even in a quantitative sense) to our simulated nanodrops at the same capillary number and static contact angle, as long as in such experiments the Reynolds number stays (well) below one. In the second place and also instigated by the need for experimental validation, studying the effects of systems where the liquids have different viscosity and/or density would be an important exercise. In the third place, the sensitivity of the current results with respect to the properties of the solid substrates needs attention. Lattice structure and lattice spacing should be varied. More importantly the assumption of nonthermal substrates as used so far requires investigation. This we will study in ways as, for example, described in Ref. 27 with the solids atoms thermally vibrating around their equilibrium position in harmonic potentials. Some preliminary single-liquid, nonequilibrium MD simulations (similar to the ones we reported for determining viscosity) including thermal walls showed virtually no effect of solids thermal motion on average liquid velocity profiles and measured viscosities up to levels of solid atom mean-square displacements that are close to melting; this finding is in line with, for example.[28]

Literature Cited

1. Nikolov A, Zhang H. The dynamics of capillary-driven two-phase flow: the role of nanofluid structural forces. *J Colloid Interface Sci*. 2015;449: 92–101.
2. Saraji S, Goual L, Piri M, Plancher H. Wettability of supercritical carbon dioxide/water/quartz systems: simultaneous measurement of contact angle and interfacial tension at reservoir conditions. *Langmuir*. 2013;29:6856–6866.
3. Zawala J, Szczepanowicz K, Warszynski P. Theoretical and experimental studies of drop size in membrane emulsification – single pore studies of hydrodynamic detachment of droplets. *Colloids Surf A*. 2015;470:297–305.
4. Kavousanakis ME, Colosqui CE, Papathanasiou AG. Engineering the geometry of stripe-patterned surfaces toward efficient wettability switching. *Colloids Surf A*. 2013;436:309–317.
5. Pappaert K, Vanderhoeven J, Van Hummelen P, Dutta B, Clicq D, Baron GV, Desmet G. Enhancement of DNA micro-array analysis using a shear-driven micro-channel flow system. *J Chromatogr A*. 2003;1014:1–9.
6. Stukan MR, Ligneul P, Boek ES. Molecular dynamics simulation of spontaneous imbibition in nanopores and recovery of asphaltenic crude oils using surfactants for EOR applications. *Oil Gas Sci Technol*. 2012;67:737–742.
7. Stukan MR, Ligneul P, Crawshaw P, Boek ES. Spontaneous imbibition in nanopores of different roughness and wettability. *Langmuir*. 2010;26:13342–13352.
8. Sui Y, Ding H, Spelt PDM. Numerical simulations of flows with moving contact lines. *Annu Rev Fluid Mech*. 2014;46:97–119.
9. Allen MP, Tildesley DJ. *Computer Simulations of Liquids*. Oxford: Clarendon Press, 1987.
10. Frenkel D, Smit B. *Understanding Molecular Dynamics*. San Diego, CA: Academic Press, 1996.
11. Alder BJ, Wainwright TE. Phase transition for a hard sphere system. *J Chem Phys*. 1957;27:1208–1209.
12. Maginn EJ, Elliott JR. Historical perspective and current outlook for molecular dynamics as a chemical engineering tool. *Ind Eng Chem Res*. 2010;49:3059–3078.
13. Palmer JC, Debenedetti PG. Recent advances in molecular simulation: a chemical engineering perspective. *AIChE J*. 2015;61:370–383.
14. Xu J, Li X, Hou C, Wang L, Zhou G, Ge W, Li J. Engineering molecular dynamics simulation in chemical engineering. *Chem Eng Sci*. 2015;121:200–216.
15. Vrabec, J, Kedia GK, Fuchs G, Hasse H. Comprehensive study of the vapour-liquid coexistence of the truncated and shifted Lennard-Jones fluid including planar and spherical interface properties. *Mol Phys*. 2006;104:1509–1527.
16. Meier K, Laesecke A, Kabelac S. Transport coefficients of the Lennard-Jones model fluid. I. Viscosity. *J Chem Phys*. 2004;121: 3671–3687.
17. Horsch M, Heitzig M, Dan C, Harting J, Hasse H, Vrabec J. Contact angle dependence on the fluid-wall dispersive energy. *Langmuir*. 2010;26:10913–10917.
18. Becker S, Urbassek HM, Horsch M, Hasse H. Contact angle of sessile drops in Lennard-Jones systems. *Langmuir*. 2014;30:13606–13614.
19. Wu X, Phan-Thien N, Fan XJ, Ng TY. A molecular dynamics study of drop spreading on a solid surface. *Phys Fluids*. 2003;15:1357–1362.
20. Hong SD, Ha MY, Balachandar S. Static and dynamic contact angles of water droplet on a solid surface using molecular dynamics simulation. *J Colloid Interface Sci*. 2009;339:187–195.
21. Busic B, Koplik J, Banavar JR. Molecular dynamics simulation of liquid bridge extensional flow. *J Non-Newtonian Fluid Mech*. 2003; 109:51–89.
22. Saavedra JH, Rozas RE, Toledo PG. A molecular dynamics study of the force between planar substrates due to capillary bridges. *J Colloid Interface Sci*. 2014;426:145–151.
23. Koplik J, Banavar JR. Molecular structure of the coalescence of liquid interfaces. *Science*. 1992;257:1664–1666.
24. Rowlinson JS, Widom B. *Molecular Theory of Capillarity*. Oxford: Clarendon Press, 1982.
25. Lion TW, Allen RJ. Computing the local pressure in molecular dynamics simulations. *J Phys Condens Matter*. 2012;24:284133.
26. ElSherbini AJ, Jacobi AM. Retention forces and contact angles for critical liquid drops on non-horizontal surfaces. *J Colloid Interface Sci*. 2006;299:841–849.
27. De Coninck J, Blake TD. Wetting and molecular dynamics simulations of simple liquids. *Annu Rev Mater Res*. 2008;38:1–22.
28. Thompson PA, Robbins MO. Simulations of contact-line motion: slip and the dynamic contact angle. *Phys Rev Lett*. 1989;63:766–769.

Manuscript received May 7, 2015, and revision received June 13, 2015.